A baseline-free and non-contact method for detection and imaging of structural damage using 3D laser vibrometry

P Aryan[1], A Kotousov[1], C T Ng[2] and B S Cazzolato1

[1]School of Mechanical Engineering, University of Adelaide, Adelaide, Australia

[2] School of Civil, Environmental & Mining Engineering, University of Adelaide, Adelaide, Australia

E-mail: pouria.aryan@adelaide.edu.au

Keywords: 3D Laser vibrometry, guided waves, structural health monitoring, damage detection, mode conversion

---

Abstract

Detection and characterisation of structural damage with guided waves is very promising in non-destructive testings and structural health monitoring systems. Due to simplicity and low cost, the current techniques normally utilise traditional piezo-electric or optic fiber sensors to capture a directional scattered field from a defect or damaged area. However, the practical implementation of these techniques usually requires an extensive preliminary study in order to identify a suitable location and polarization of the sensors, as well as optimal parameters for wave excitation, which vary depending on the size and type of the damage and structure. The recent advances in 3D laser vibrometry provided an opportunity to avoid many restrictions and limitations associated with the traditional (1D) sensing systems by capturing the transient 3D displacement/velocity fields rather than signal in several discrete locations. Based on the recent advances in 3D lase vibrometry this paper suggests a non-contact baseline-free method for imaging structural defects such as corrosion spots, cracks, and dents as well as delamination damage. It focuses on the mode conversion effects and investigates the sensitivity of the in-plane and out-of-plane scattering fields to the presence of the common defects. The experimental measurements are presented in terms of root mean square (RMS) values of the velocity field. The outcomes of the present study can help, for example, in selecting an appropriate strategy for defect detection using guided wave techniques.

1. Introduction

Guided waves have the ability to propagate over large distances without significant energy decay and are found to be very sensitive to the presence of various types of structural defects, such as fatigue cracks, delamination damage or corrosion spots [1-6]. In recent years guided waves have been successfully employed in the development of effective structural health monitoring techniques across many industries and applications [7-11].

A variety of sensors are currently used to detect the scattering characteristics of guided waves. Piezo-elements (PZ) and optical fibre (OF) sensors are presently most common due to their low cost, small size and light weight, as well as high sensitivity to stress waves [1, 2, 7, 8, 12]. However, the application of these sensors for damage detection often requires extensive preliminary experimental or numerical studies in order to identify the suitable location, polarisation and other characteristics of the sensor array, as well as determine appropriate wave modes and excitation frequency for a reliable detection of the targeted damage or structural defects [13-15]. This could be a formidable task if several types or various sizes of defects or damage are targeted.

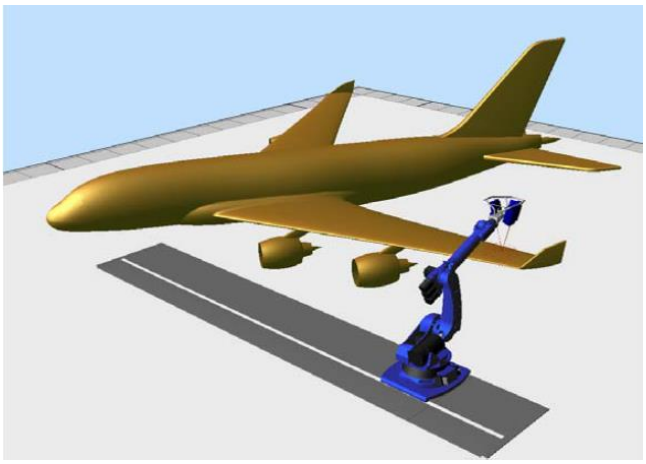

Figure 1: Illustration of a 3D SLV mounted on a ganty-operated, seven degree-of-freedom serial manipulator.

The development of 3D scanning lased vibrometry (3D SLV) over the past fifteen years has provided a non-invasive, non-contact, highly accurate tool to the guided wave characterisation [16, 17]. The cost and weight of 3D SLV systems are currently the main constraints for potential practical applications. However, these will be eventually decreased with the rapid advance in the technology, and the utilisation of 3D laser vibrometry in

industrial applications is just a matter of time. One envisages that such a system, for example, could form a non-contact platform for aircraft non-destructive inspection as illustrated in Fig.1.

In addition to the ability to measure full 3D displacement or velocity fields, 3D SLV systems have many other advantages over the conventional sensor elements including a superior spatial resolution, better accuracy and the non-contact nature of the measurements, so it eliminates the influence of the conventional contact transducers on the test object motion dynamics. The use of SLV technology naturally avoids many obstacles associated with the traditional sensing elements (PZT or FO), such as a need for a high fidelity baseline signal or compensation systems to avoid effects of temperature change or applied loading.

In a number of recent studies, SLV systems were applied to detect and visualise damage in both metallic and composite components [18-23]. In particular, the SLV systems were employed to create wavefield images around structural defects with a high spatial resolution [21, 24-26] as well as experimentally investigate the mode conversion effects as a result of wave scattering from various types of defects [27-29]. In addition, advanced signal and post processing techniques were developed over the past five years to improve the accuracy and resolution of structural defect imaging systems based on 1D and 3D SLV [26, 30-33].

The purpose of this paper is to present a baseline-free and non-contact method for detecting and imaging defects in structures based on the evaluation of the root mean square values (RMS) of the velocity fields of guided waves in a time window using advanced 3D SLV. It is demonstrated that the RMS provides a simple and effective way for imaging and sizing various structural defects. The sensitivity of the in-plane and out-of-plane scattered velocity fields of guided waves to the presence of typical defects as well as mode conversion affects generated by various types of structural defects are also investigated.

2. Experimental approach

This section describes the details of the specimens, and the set-up utilised for the experimental investigations. The guided wave measurement system consists of a Polytec PSD-3D 400 SLV (with three separate laser heads, a computer and a built-in function generator), power amplifier, test specimen and PZT transducer as illustrated in Fig. 2.

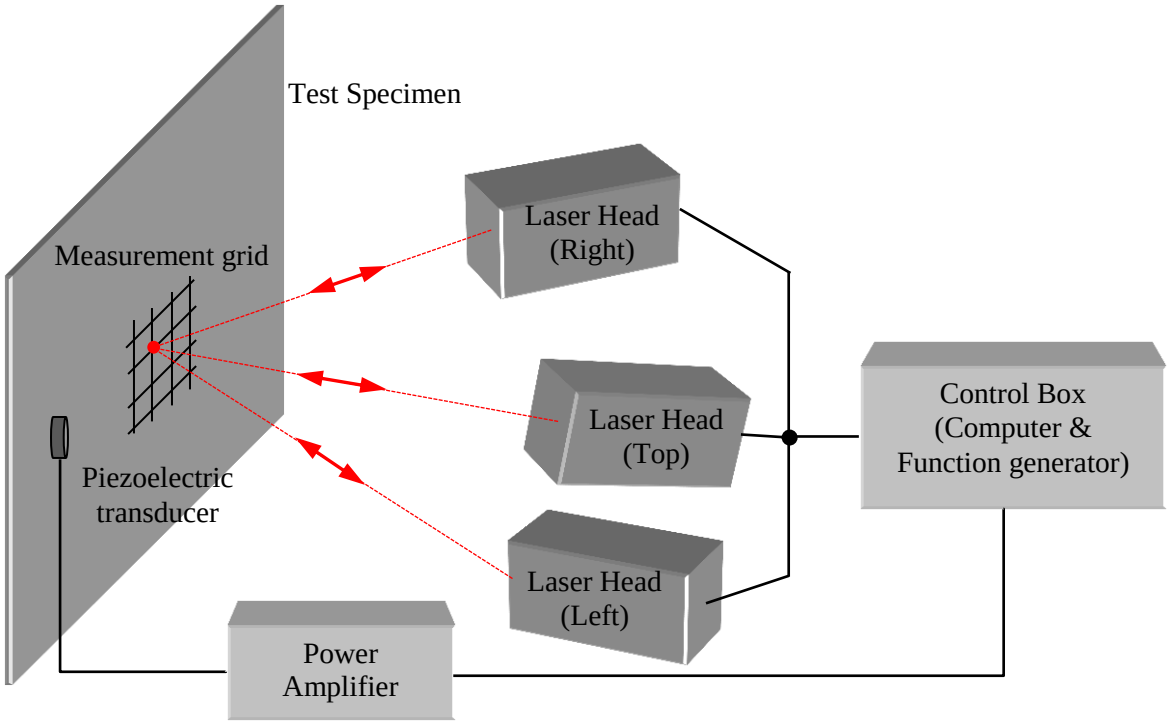

Figure 2: Schematic illustration of the experimental arrangement for measurement of the velocity fields on a flat plate over the specified damage area using 3D SLV.

2.1 Test specimens

Three different test specimens with typical structural defects were fabricated from large aluminium plates, with in-plane dimensions of 400 mm by 800 mm and 3 mm thickness. The plate dimensions were selected to avoid the effect of wave reflections from plate's boundaries on the imaging and mode conversion within a short time window used for measurements. A blind hole of 1.5 mm depth and 10 mm diametre representing a corrosion type defect was milled in the first plate. A surface crack of 10 mm length and 1.5 mm depth was introduced in the second plate and three different dents of 1mm, 2mm and 3mm in diametre were fabricated in the third aluminium plate specimen.

In addition to the aluminium plate specimens, an 8-ply carbon fibre reinforced composite beam, with dimensions of 285mm by 12mm by 2 mm and a hidden delamination located between the 3rd and 4th layer was fabricated. The delamination is one of the most common damages in composites due to low transverse strength and fracture toughness. In composite components the delamination can be caused during manufacture or during service. The manufacturing defects often occur due to improper lamination and curing processes or may be introduced by machining the components for fastener holes and design cut-outs etc. The service damage may result from the impact by runway debris, hailstones, bird strike, ground service vehicles, ballistics etc. In many instances, the damage caused by such impacts may not be visible or barely visible on the surface but may significantly reduce the strength of the structural component. Therefore, the availability of practical and robust non-destructive evaluation techniques for damage detection and monitoring is critical to ensure the acceptable performance of structures in terms of serviceability, reliability, durability, and prevention of catastrophic failures. The composite specimen is shown in Fig. 3.

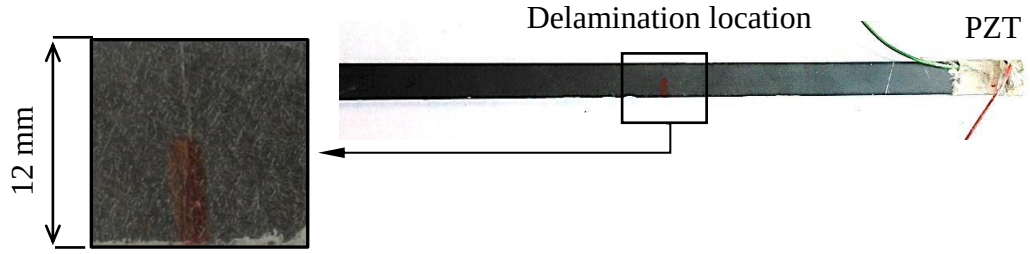

Figure 3: Photograph of the carbon fibre reinforced composite beam specimen with a delamination used in this study.

2.2 Experimental set-up

A Polytec PSV 400 3D SLV was used to measure the structural response of the test specimens. The PSV 400 3D and a plate specimen is shown in Fig. 4. To generate the guided waves, a five and a half cycle Hanning windowed tone burst signal, at frequencies between 100 - 300 kHz with a 50 kHz increasing step, was used. The tone bursts are generated by the Polytec PSV-3D SLV built–in signal generator and amplified up to ±50 V using a power amplifier to drive a piezoelectric transducer (PZT). Two types of PZT transducers were used for the specimens in the current study. For the plates, a disk-shaped PZT with dimensions of

10 mm in diametre and 2 mm thickness with backing mass of 10 mm in diametre and 3 mm thickness made of brass. For the composite beam, a rectangular–shaped PZT with the dimensions of 6mm by 12 mm and 2 mm thickness with a backing mass of 6mm by 12 mm and 3 mm thickness made of brass was used. The PZTs convert the amplified electrical signal from the amplifier to surface displacements that generate the guided waves in the specimens.

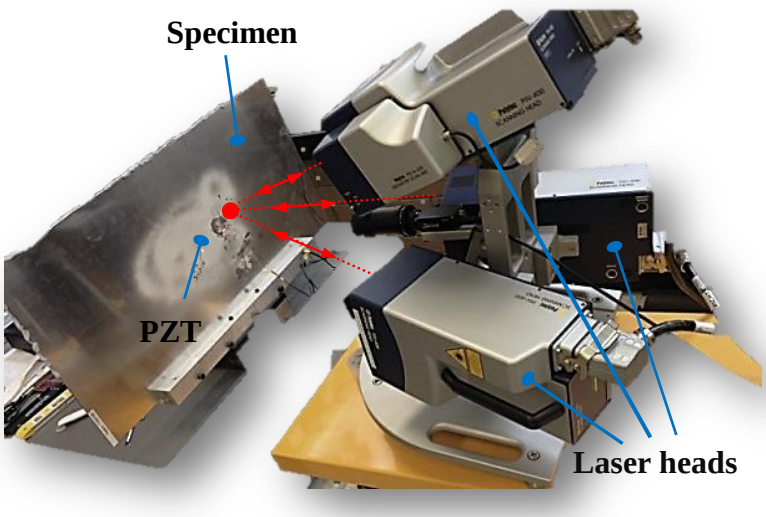

Figure 4: Polytec PSV-3D SLV and experimental set-up

The velocity components were measured at grid points in a rectangular area covering the defects and the surroundings surface region, see Fig. 2. In order to achieve a high quality resolution image of the wave propagation in the structure, a sufficiently small uniform measurement grid size was selected to ensure there are at least 8 measurement points exist per wavelength of the incident A_o guided wave. To improve the signal-to-noise ratio (SNR) 200 time responses were averaged for each measurement point. Band pass filters, with lower and higher cut off frequencies based on the signal envelope energy of each centre frequency, was applied to reduce the measurement noise outside of the frequency band (e.g. $\pm$50 kHz for 200 kHz excitation frequency). A sampling rate of 1.5 MHz was used for in all experimental measurements.

3. Results and discussions

This section describes the outcomes of the experimental study on scattering Lamb waves from the typical structural defects as described in the previous section. The results are presented in terms of Root Mean Square of the velocity field components. Further, we will analyse these results in order to develop an effective strategy for detection and imaging of various defects.

3.1 Wave scattering at blind hole

The fundamental A_o guided wave mode was excited and facilitated by the use of a backing mass within the designated frequency range from 100 to 300 kHz. This mode largely produces out-of-plane displacements, or V_Z-components and the magnitude of the two other velocity components in the incident wave field are very small. The PZT was mounted 70 mm from the blind hole with characteristic dimensions as described in the previous section.

The wave propagation in structure is shown in Fig. 5. The snap-shots in this figure represent the out-of-plane velocity field (or V_Z-component) at different times. The actual location and size of the blind hole in is marked with a circle. The presence of the hole can be identified directly from these pictures. However, to improve the visualisation and characterisation of the defect, the experimental measurements were represented in terms of the RMS of the velocity fields.

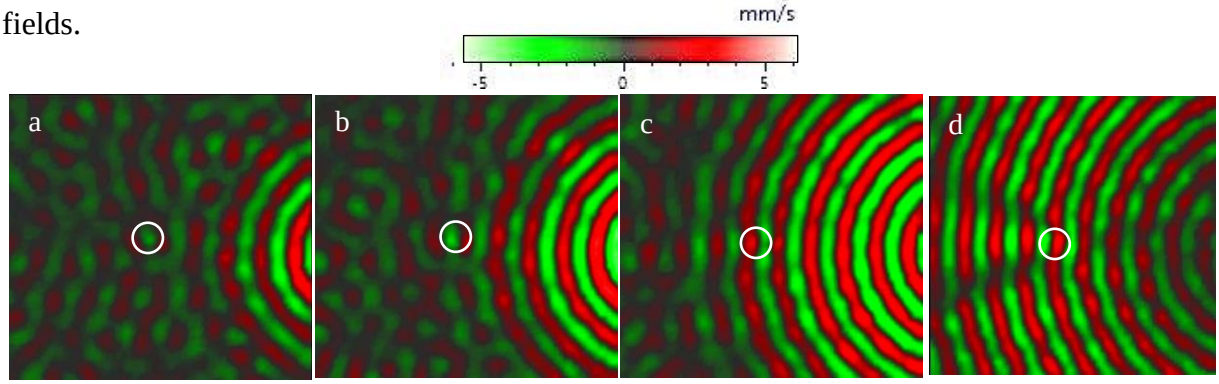

(a) 23.83μs (b) 30.08μs (c) 39.45μs (d) 54.69μs

Figure 5: Snap shots of V_Z-component (out-of-plane) at 200 kHz. The size and location of the blind hole is marked by a circle.

To visualise the damage and investigate the sensitivity of the in-plane and out-of-plane scattered fields to the presence of various types of damage and defects, the RMS of velocity fields were calculated from the experimental measurements. There are various types of average measure can be utilised depending on the situation. The RMS is also is a type of average measure that provides an average value of the magnitude of a variable (time variable

in this case). RMS can be calculated for a series of discrete values or for a function. RMS calculation represents an average measure, which eliminates the difference between negative and positive magnitudes of the mesured values. In the case of a discret set of n values, $\{a_1, a_2, a_3, \dots, a_n\}$, the RMS value is given by [34].

$$a_{RMS} = \sqrt{\frac{1}{n}(a_1^2 + a_2^2 + \cdots + a_n^2)} \tag{1}$$

Important features of the RMS, also known as quadratic mean, are that the RMS over all time of a periodic function is equal to the RMS of one period of the function, and the RMS value of a continuous function or signal can be approximated by taking the RMS of a series of equally spaced samples, which is important for the current study. For the three components of the velocity fields, $\mathrm{V_X}(t, \mathrm{x}, \mathrm{y}), \mathrm{V_Y}(t, \mathrm{x}, \mathrm{y})$ and $\mathrm{V_Z}(t, \mathrm{x}, \mathrm{y})$. The RMS field (continous or at discrete points) can be calculated as:

$$\mathrm{RMS} = \sqrt{\left(\sum_{n=1}^{n_S} V_n^2\right) \Big/ (n_S)} \quad , \tag{2}$$

where V_n are the magnitudes of the velocities in time domain and n_S is number of samples. In this study 2048 samples were taken for each measurement point at 2.5 MHz and in 819.2 µsec of time window. The measument grid density was set to approximately 10 points per wavelength of the excited $\mathrm{A_o}$ mode.

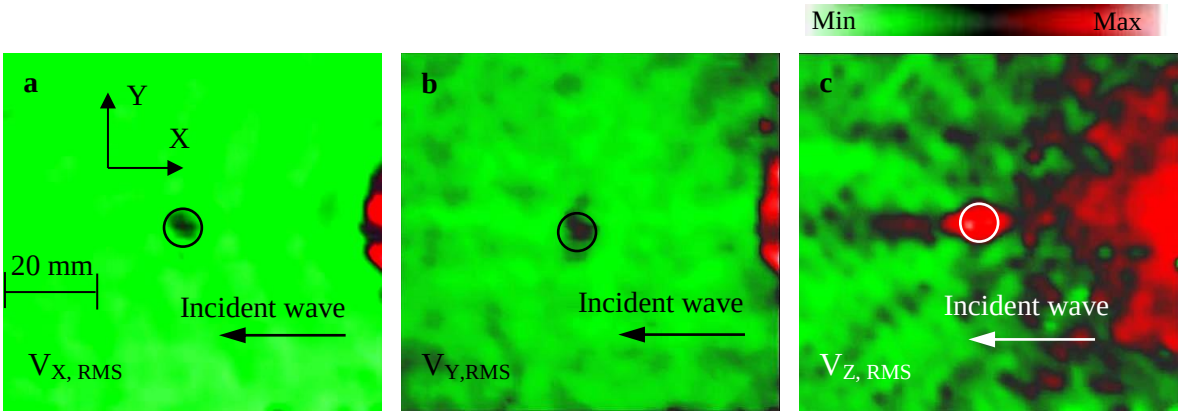

Figure 6: RMS of the velocity field components for the blind hole in a) *x*, b) *y* and c) *z* (out-of-plane) directions at 200 kHz, where *x*-direction is aligned with the direction of the incident wave. The circle represents the size and the location of the blind hole.

The RMS of *x*, *y* and *z*-components of the surface velocity field are shown in Fig. 6. In this figure the location of the damage is clearly visible from this figure. The right hand side of the figures is disturbed by the reflected wave due to a relatively short distance between the PZT and the blind hole. Further effort was undertaken to identify the characteristic sizes of the observed damage.

Fig. 7 shows the RMS values plotted along two lines passing through the centre of the hole: one in direction of the incident wave (*x*-direction) and transverse direction (*y*-direction). The actual location of the hole in these diagrams is indicated by dotted lines.

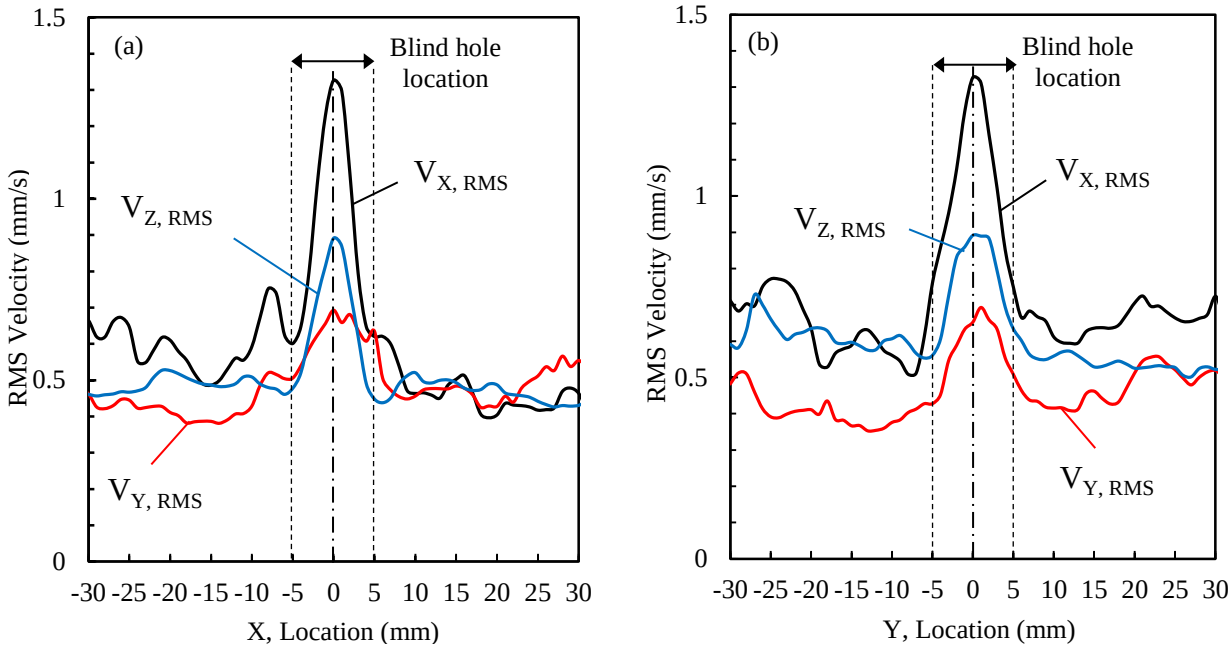

Figure 7: Section views of RMS of the velocity fields along (a) the *x*-direction and (b) *y*-direction through the centre of blind hole

As can be observed in this figure, the diametre of the hole can be identified from the RMS plots with any component of the scattered 3D velocity field. From a comparison of the RMS values, it can be concluded that the in-plane x-velocity component of the scattered field, which is a result of mode conversion, is the most sensitive to the presence of the blind hole. It is interesting to note that the section views of the *x*-and *y*-directions have very similar patterns of the RMS value. The above conclusion, for instance, can be quite useful in the selection of defect detection strategies with guided wave techniques for identification and characterisation of corrosion type damage.

3.2 Wave scattering at crack

A similar analysis was conducted for the second specimen. Different time snapshots of the out-of-plane velocity field (V_Z) around the crack described in the previous section are shown in Fig. 8. The location of the crack is marked by an ellipse. The corresponding RMS of velocity fields of the three components are shown in Fig. 9. The PZT is located 70 mm from the crack as before and the disturbance on the right hand side of Fig. 9 is due to the effect of the reflected wave.

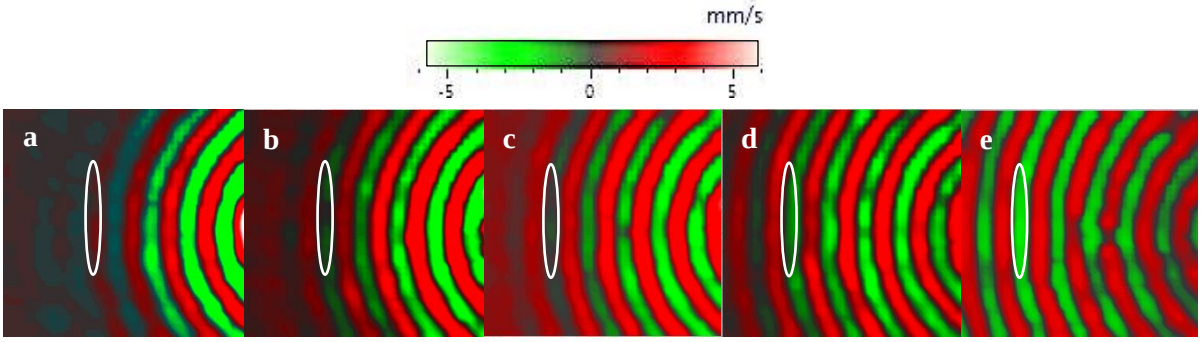

(a) 30.08µs (b) 32.20 µs (c) 35.40 µs (d) 40.69µs (e) 46.20µs

Figure 8: Snap shots of the V_Z-component (out-of-plane) at 250 kHz. Location and size of the crack is marked by a white ellipse.

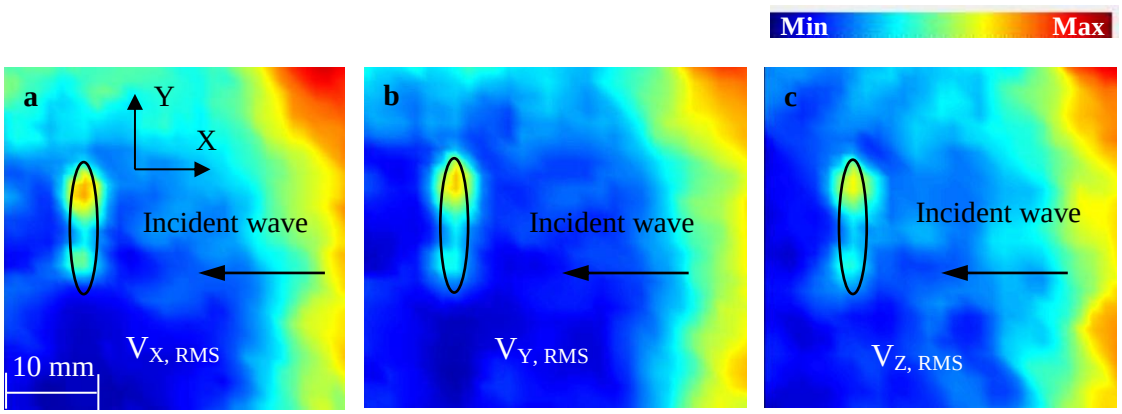

Figure 9: RMS of the velocity field components for the crack in a) *x*, b) *y* and c) *z* (out-of-plane) directions at 250 kHz, where x-direction is aligned with the direction of the incident wave. The ellipse marks the location and size of the crack.

Further, Fig. 10 shows the results of the RMS of the scattered fields along two lines passing through the centre of the crack: one in direction of the incident wave (*x*-direction) and the

other in the transverse direction (*y*-direction). The size and location of the crack in these diagrams is indicated by dotted lines.

The results are different to the previous case. In the case of the crack defect, the sensitivity of the in-plane velocity components ($V_{X,\ RMS}$ and $V_{Y,\ RMS}$) are quite similar and much more sensitive to the presence of this structural defect than $V_{Z,\ RMS}$. The length of the crack (10 mm) is not easily identified from the directional RMS plots presented in Fig. 10. From a comparison with the previous results it is difficult to distinguish between these types of structural damage since they have very similar characteristics in terms of mode conversion and the intensities. One distinct feature is a much lower sensitivity of $V_{Z,\ RMS}$ to the presence of crack damage in comparison with the blind hole (corrosion type) damage.

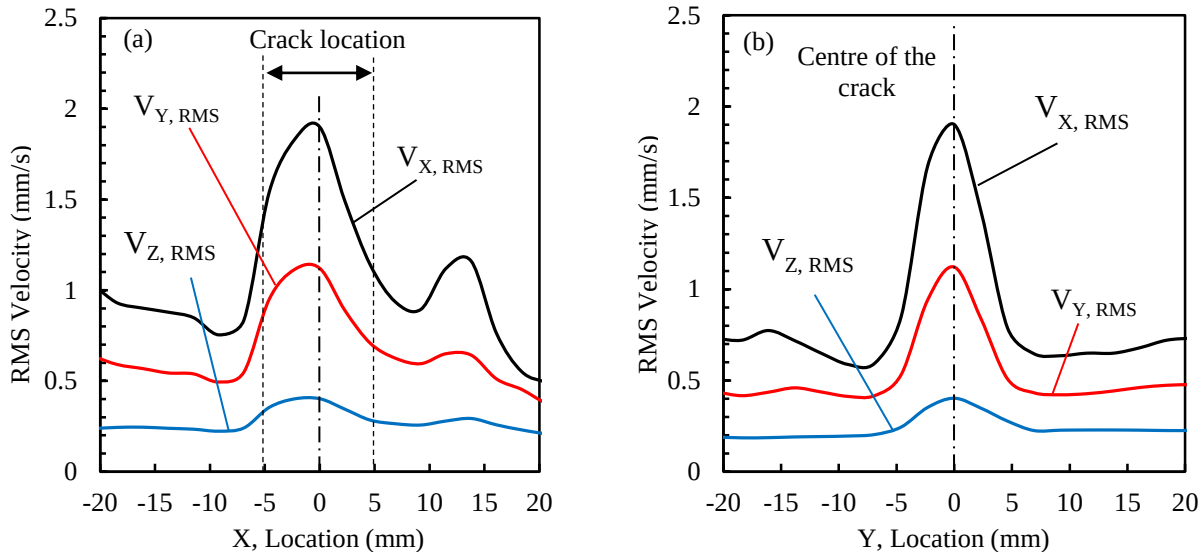

Figure 10: Section views of RMS of the velocity fields along the (a) the *x*-direction and (b) *y*-direction through the centre of the crack

3.3 Wave scattering for dents

The wave scattering from the dents of three different sizes (1mm, 2mm and 3mm diametres) was investigated with the 3D SLV. Similar to the previous cases, the fundamental A_o guided wave mode was excited with the PZT transducer. The guided wave propagation and selected snapshots of the out-of-plane velocity field across the surface of the plate are presented in Fig. 11.

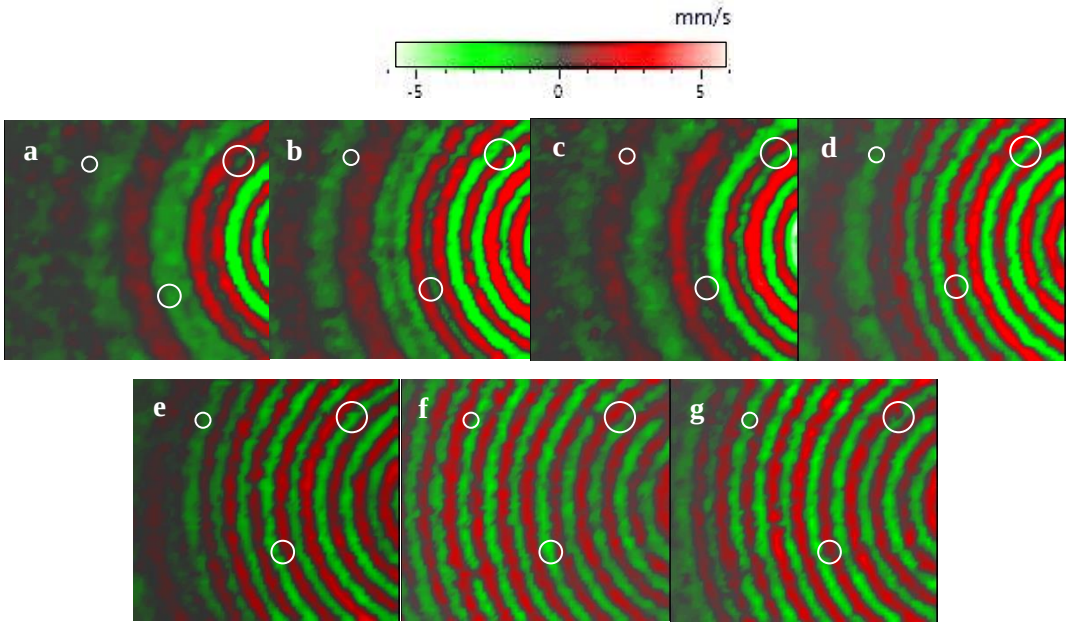

Figure 11: Snap shots of V_Z-component (out-of-plane) at (a) 30.25µs (b) 34.30µs (c) 38.28µs (d) 42.03µs, (e) 48.05µs, (f) 51.95µs and (g) 57.42µs at 250 kHz. The sizes and locations of the dents are marked by different sized circles.

The corresponding RMS of the velocity fields along the incident wave direction and the transverse direction are presented in Fig. 12. The locations of the dents are marked by different sizes of circles and the high values appeared at the locations of the dents in all three RMS components.

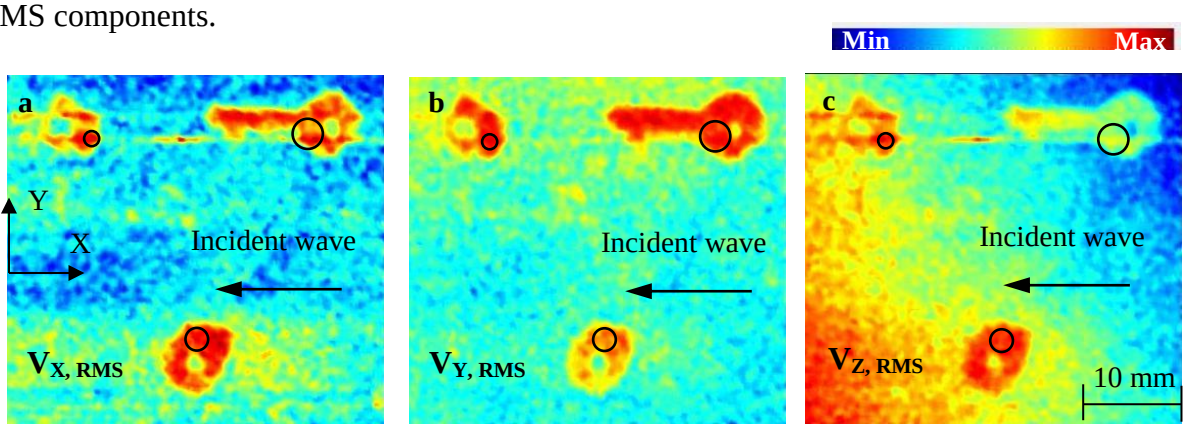

Figure 12: RMS of the velocity field components for the dents in a) *x*, b) *y* and c) *z* (out-of-plane) directions, where the *x*-direction is aligned with the direction of the incident wave.

In Fig. 13 the RMS values of all velocity components are plotted along two directions cut through the centres of the dents parallel and transverse to the direction of the incident wave.

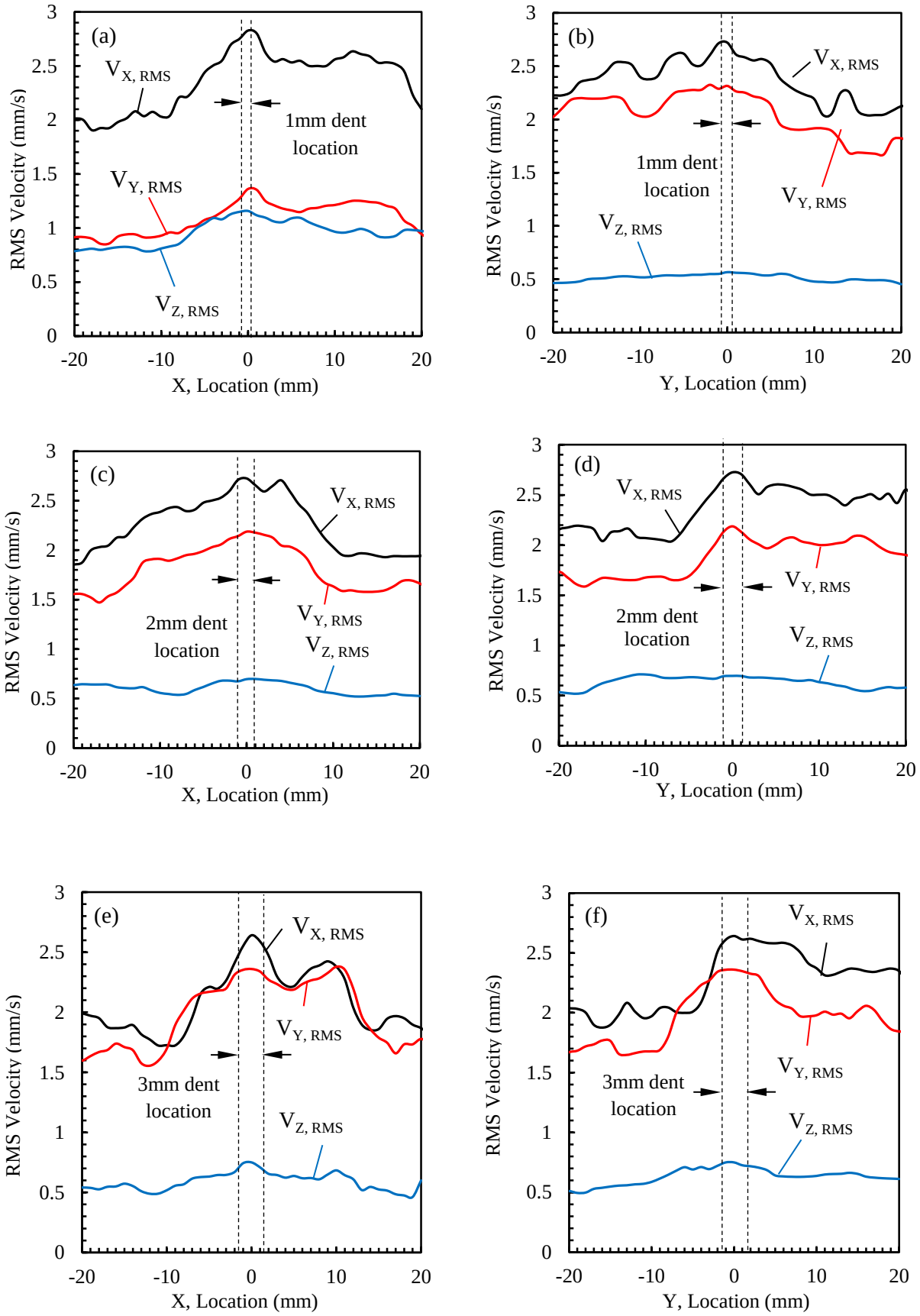

Figure 13: Section views of RMS of the velocity fields along the *x*-direction and *y*-direction through the centre of the dents with 1mm diametre (a & b), 2mm diametre (c & d) and 3mm diametre (e & f).

The results presented in Fig. 13, indicate that the $V_{Z,\ RMS}$ values are not sensitive to the presence of the dents of the specified sizes. However, this type of damage can be characterised with $V_{X,\ RMS}$ and $V_{Y,\ RMS}$ fields. The values, plotted along the *x*-direction and *y*-direction, clearly indicate the presence of all three dents.

For all three dents, the amplitudes of the RMS of the velocity fields of the in-plane components were higher than RMS of the out-of-plane component. As a result, for the plate with the dents the in-plane scattered field was also found to be more sensitive to this type of defect rather than the out-of-plane component of the velocity field. This observation is very similar to the case of the blind hole and crack considered earlier.

3.4 Wave scattering at a delamination

Finally, the fundamental guided wave mode (A_o) at 200 kHz was excited for the case of the carbon fibre reinforced composite beam specimen with a delamination defect as described in the previous section (see Fig. 2). Similar to the previous results, the snap shots of the z-velocity component are shown in Fig. 13. The RMS fields of these velocity components are presented in Fig. 14. This figure clearly demonstrates the advantages using the RMS to characterise the wave scattering as it provides a much better signature of the defect.

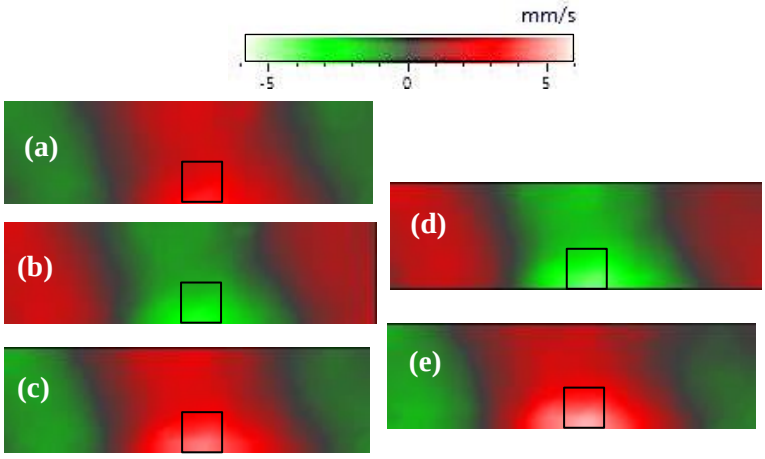

Figure 13: Snap shots of V_Z-component (out-of-plane) at (a) 46.35μs (b) 49.62μs (c) 51.28μs (d) 54.03μs and (e) 57.05μs at 200 kHz. The location of the delamination is marked.

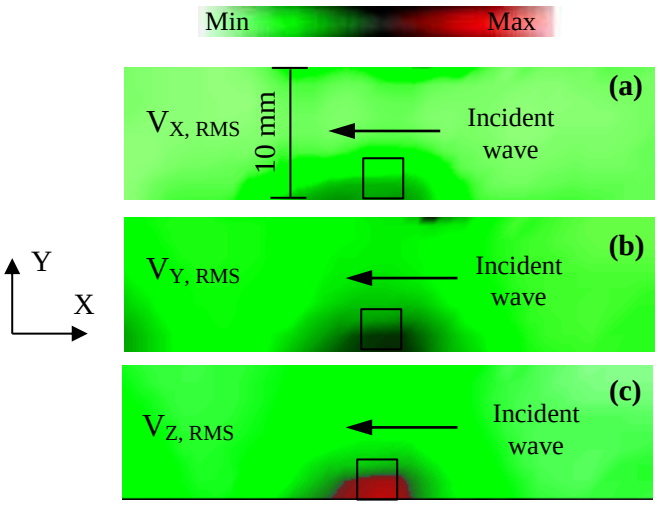

Figure 14: RMS of the velocity fields components for the hidden delamination in (a) *x*, (b) *y* and (c) *z* components. The location of the delamination is marked.

The RMS values along two lines passing through the centre of the defect parallel and perpendicular to the incident wave direction are provided in Fig. 15. From a comparison of the RMS for different components, it can be concluded that the in-plane velocity *y*-component of the scattered field is the most sensitive to the presence of the hidden delamination damage.

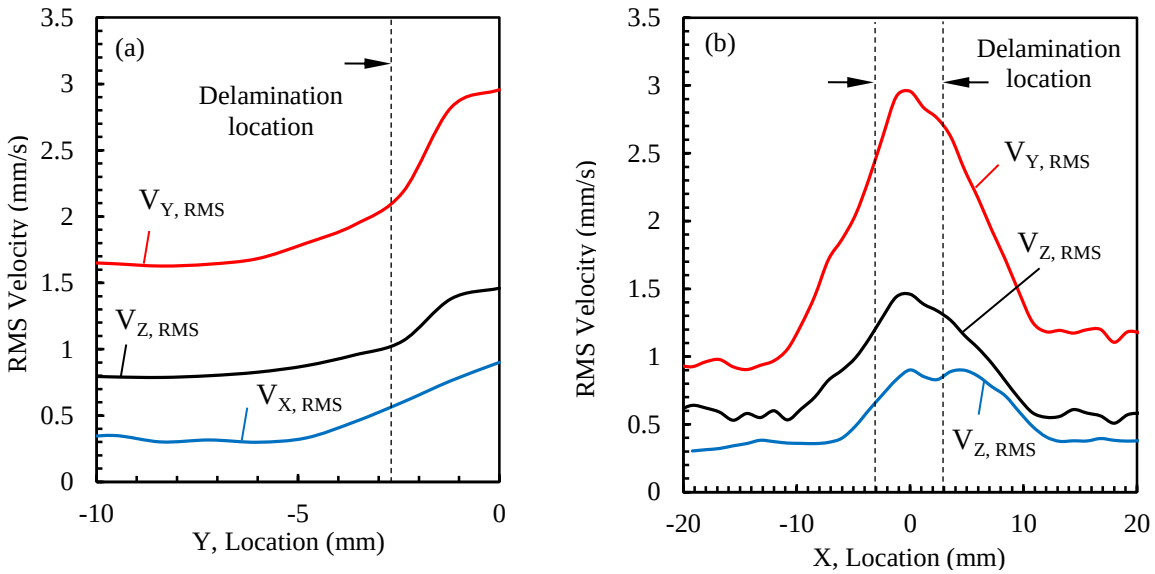

Figure 15: Section views of the RMS of the velocity fields along the (a) transverse direction and (b) incident wave directions for hidden delamination in the carbon fibre reinforced composite beam.

All the RMS curves corresponding to different velocity components clearly indicate the boundaries of the delamination. It is interesting to note that both the incident wave and transverse directions provide very similar patterns and can be utilised for the detection and

sizing this type of damage. The outcomes of this analysis can also be useful in the selection of the strategy of composite delamination detection with guided wave techniques, in particular, sensor polarisation and their locations with respect to expected damage.

The outcomes of this experimental investigation on damage detection and imaging with 3D laser vibrometry generally confirms the results of numerous previous studies utilising 1D and 3D laser vibrometry [18, 20, 27, 29]. Specifically, that the wave responses from various types of damage can be reliably acquired using SLV and that the post-processing stage of the measured data is one of the crucial elements in damage imaging [24]. Proper interpretation of SLV data scans can lead to a more clear understanding of Lamb wave propagation and also improve the understanding of the mode conversion effect as well. This can significantly affect damage detection and imaging methods using laser vibrometry. Many recent studies have indicated that the move from 1D to 3D measurements will enable the register of not only anti-symmetric waves but also symmetric and even shear horizontal waves due to mode conversion effect [35]. The current work is partially motivated by these expectations and represents a study on 3D wave scattering of Lamb waves and defect imaging utilising the RMS of the 3D velocity field components instead of just 1D at typical structural defects. The main outcomes of this work, which highlight this step as well as the differences between 1D and 3D laser vibrometry, are summarised in the Conclusions section of this paper.

4. Conclusions

In this paper, a non-contact technique for imaging defects in various structures based on the 3D measurements conducted with a 3D SLV was presented. In all cases the fundamental A_o guided wave mode was excited, which prevent the generation of higher order harmonics. The mode conversion effects and the sensitivity of the in-plane and out-of-plane components of the scattered filed to the presence of different types of mechanical defects were investigated. It is believed that the selected dimensions of the structural damage do not significantly affect the main outcomes of the experimental work, which can be summarised as follows:

(1) The conducted investigations confirmed that use of RMS values of the velocity components without the need of baseline information, provide good quality damage signatures for all considered structural defects;

(2) For all considered types of structural damage the RMS values of the mode converted in-plane velocity components (V_X and V_Y) were found to be much more sensitive to the presence of the defects than the out-of-plane velocity components (V_Z);

(3) The sensitivity of the RMS of the velocity components to the presence of the damage along different directions (parallel or transverse to the incident wave propagation) was found to be quite similar for each case study. For all the aluminium specimens, it has been found *x*-components are much more sensitive while for the delamination defect the *y*-component is more sensitive, in the composite beam case study;

(4) It is still difficult to distinguish between the damage signatures of the blind hole and crack. One feature, which is quite promising and needs to be further investigated, is a much lower sensitivity of the $V_{Z,\,RMS}$ to the presence of cracks;

(5) The outcomes of the present experimental study clearly demonstrate the advantages of capturing the full 3D in the detection, characterisation and sizing of the mechanical structural damage.

A summary of the main outcomes of this experimental study is presented in Table 1. The table shows the normalised peak levels by spatial RMS level for all the cases of structural damage considered in this paper. The signal ratio is calculated as the ratio of the maximum RMS of the velocity components to the spatial average RMS of the components. The signal ratio is specified as

$$SR_\beta = \frac{\mathrm{Max}(V_{\beta,RMS})}{\mathrm{Average}(V_{\beta,RMS})} \tag{3}$$

where β represents x, y or z.

Table 1. SR_β for different velocity components along the incident wave and transverse directions for all the different types of damage considered.

Damage type		Parallel with incident wave direction			Transverse with incident wave direction		
		SR_x	SR_y	SR_z	SR_x	SR_y	SR_z
Blind hole		2.30	1.40	1.80	1.80	1.40	1.50
Crack		2.30	1.40	1.80	1.80	1.40	1.50
Dents	1mm	1.21	1.20	1.20	1.29	1.22	1.28
	2mm	1.18	1.18	1.11	1.22	1.22	1.15
	3mm	1.18	1.15	1.12	1.29	1.22	1.20
Delamination		1.72	1.73	1.67	1.73	1.48	1.50

The ratio was calculated parallel and perpendicular to incident wave direction. As it can be seen from Table 1, the SR_x values are normally higher in comparison with the other directional components.

Acknowledgements

This work was partially supported by the Australian Research Council under grant number DE130100261.

References

1. Rose JL. A baseline and vision of ultrasonic guided wave inspection potential. *Journal of Pressure Vessel Technology* 2002; **124**(3): 273-282.
2. Su Z, Ye L, Lu Y. Guided Lamb waves for identification of damage in composite structures: A review. *Journal of Sound and Vibration* 2006; **295**(3–5): 753-780.
3. Ng CT, Veidt M. Scattering characteristics of Lamb waves from debondings at structural features in composite laminates. *The Journal of the Acoustical Society of America* 2012; **132**(1): 115-123.
4. Yao Y, Tung S T E, Glisic B. Crack detection and characterization techniques—An overview. *Structural Control and Health Monitoring* 2014; **21**(12):1387-1413.
5. Sharma S, Mukherjee A. Ultrasonic guided waves for monitoring corrosion in submerged plates. *Structural Control and Health Monitoring* 2015; **22**(1):19-35.
6. Yeum, C M , Sohn H, Lim H J, Ihn J B. Reference-free delamination detection using Lamb waves. *Structural Control and Health Monitoring* 2013; **21**(5): 675-684.
7. Duflo H, Morvan B, Izbicki JL. Interaction of Lamb waves on bonded composite plates with defects. *Composite Structures* 2007; **79**(2): 229-233.
8. Ng CT, Veidt M. A Lamb-wave-based technique for damage detection in composite laminates. *Smart Materials and Structures* 2009; **18**(7): 74006-74018.
9. Tian Z, Leckey C, Rogge M, Yu L. Crack detection with Lamb wave wavenumber analysis. *Health Monitoring of Structural and Biological Systems* 2013; 86952Z-1-86952Z-13.
10. Ge L, Wang X, Jin C. Numerical modelling of PZT-induced Lamb wave-based crack detection in plate-like structures. *Wave Motion* 2014; **51**(6): 867-885.
11. Ng CT. Bayesian model updating approach for experimental identification of damage in beams using guided waves. *Structural Health Monitoring* 2014; **13**(4):359-373.
12. Sbarufatti C, Manes A, Giglio M. Application of sensor technologies for local and distributed structural health monitoring. *Structural Control and Health Monitoring* 2014; **21**(7):1057-1083.
13. Lowe MJS, Cawley P, Kao JY, Diligent O. The low frequency reflection characteristics of the fundamental antisymmetric Lamb wave Ao from a rectangular notch in a plate. *The Journal of the Acoustical Society of America* 2002; **112**(6): 2612-2622.
14. Ng CT, Veidt M, Rose LRF, Wang CH. Analytical and finite element prediction of Lamb wave scattering at delaminations in quasi-isotropic composite laminates. *Journal of Sound and Vibration* 2012; **331**(22): 4870‑4883.
15. Lowe MJS, Cawley P, Kao JY, Diligent O. The low frequency reflection characteristics of the fundamental antisymmetric Lamb wave Ao from a rectangular notch in a plate. *The Journal of the Acoustical Society of America* 2002; **112**(6): 2612-2622.
16. Cazzolato B, Wildy S, Codrington J, Kotousov A, Schuessler M. Scanning laser vibrometer for non-contact three-dimensional displacement and strain measurements. *Proceedings of the Australian Acoustical Society Conference Geelong Australia* 2008.

17. Weisbecker H, CazzolatoB, Wildy S, Marburg S, Codrington J, Kotousov A. Surface strain measurements using a 3D scanning laser vibrometer. *Experimental mechanics* 2012; **52**(7): 805-815.
18. Swenson ED, Sohn H, Olson SE, Desimio MP. A comparison of 1D and 3D laser vibrometry measurements of Lamb waves. *SPIE Smart Structures and Materials and Nondestructive Evaluation and Health Monitoring* 2010; **7650**(0): 765003-1-765003-11.
19. Adams D, Koester D, Underwood S. Damage detection using laser vibrometry. *2nd International Symposium on NDT in Aerospace* 2010 - Mo.4.A.2.
20. Park B, An YK, Sohn H. Visualization of hidden delamination and debonding in composites through noncontact laser ultrasonic scanning. *Composites Science and Technology* 2014; **100**(0): 10-18.
21. Sohn H, Swenson ED, Olson SE, DeSimio MP, Dutta D. Delamination detection in composite structures using laser vibrometer measurement of Lamb waves. *SPIE Smart Structures and Materials and Nondestructive Evaluation and Health Monitoring* 2012; **7650** (0): 76500P-1- 76500P-10.
22. Aryan P, Kotousov A, Ng CT, Cazzolato B. Characterisation of Lamb waves with 3D laser vibrometry. *International Conference on Structural Integrity and Failure Melbourne, Australia* 2013.
23. Chia C C, Jeong H M, Lee J R, Park G. Composite aircraft debonding visualization by laser ultrasonic scanning excitation and integrated piezoelectric sensing. *Structural Control and Health Monitoring* 2012; **19**(7): 605-620.
24. Staszewski W, Lee B, Traynor R. Fatigue crack detection in metallic structures with Lamb waves and 3D laser vibrometry. *Measurement Science and Technology* 2007; **18**(3): 727-739.
25. Sohn H, Dutta D, Yang J Y, Park H J, DeSimio M, Olson S, Swenson E. Delamination detection in composites through guided wave field image processing. *Composites Science and Technology* 2011; **71**(9): 1250-1256.
26. Sohn H, Dutta D, Yang J Y, DeSimio M, Olson S, Swenson E. Automated detection of delamination and disbond from wavefield images obtained using a scanning laser vibrometer. *Smart Materials and Structures* 2011; **20**(0): 045017-045027.
27. Willberg C, Mook G, Pohl J, Gabbert U. Laser-vibrometric measurement and numerical modeling of local and continuous mode conversion of Lamb waves in CFRP Plates. *6th European Workshop on Structural Health Monitoring* 2012.
28. Schubert L, Barth M, Klesse T, Köhler B, Frankenstein B. Guided elastic waves and their impact interaction in CFRP structures characterized by 3D laser scanning vibrometry. *Health Monitoring of Structural and Biological Systems Tribikram KunduSan Diego, California* 2008.
29. Pohl J, Mook G. Laser-vibrometric analysis of propagation and interaction of Lamb waves in CFRP-plates. *CEAS Aeronautical Journal* 2013; **4**(1): 77-85.
30. Willberg C, Koch S, Mook G, Pohl J, Gabbert U. Continuous mode conversion of Lamb waves in CFRP plates. *Smart Materials and Structures* 2012; **21**(7): 075022-075031.
31. Ruzzene M. Frequency–wavenumber domain filtering for improved damage visualization. *Smart Materials and Structures* 2007; **16**(6): 2116-2123.
32. Michaels TE, Michaels JE, Ruzzene M. Frequency–wavenumber domain analysis of guided wavefields. *Ultrasonics* 2011; **51**(4): 452-466.
33. Michaels TE, Ruzzene M, Michaels JE. Incident wave removal through frequency wavenumber filtering of full wavefield data. *AIP Conference Proceedings* 2009.

34. Alexander C, Sadiku M. Fundamentals of Electric Circuits. *McGraw-Hill Science/Engineering/Math* 5th ed. 2012.
35. Malinowski P, Wandowskia T, Kudelaa P, Ostachowicza W. Laser vibrometry for guided wave propagation phenomena visualisation and damage detection. *AIP Conference Proceedings* 2010.